

**Crystal reorientation in methylammonium lead iodide perovskite thin film with thermal annealing**

| | |
|-------------------------------|----------------------------------------------------------------------------------------------------------------------------------------------------------------------------------------------------------------------------------------------------------------------------------------------------------------------------|
| Journal: | <i>Journal of Materials Chemistry A</i> |
| Manuscript ID | TA-ART-03-2019-002358.R1 |
| Article Type: | Paper |
| Date Submitted by the Author: | 08-Apr-2019 |
| Complete List of Authors: | Kavadiya, Shaline; Arizona State University Strzalka, Joseph; Argonne National Laboratory, Building 432 Niedzwiedzki, Dariusz; Washington University in St Louis, Photosynthetic Antenna Research Center (PARC) Biswas, Pratim; Washington University in St Louis, Energy, Environmental and Chemical Engineering |
| | |

ARTICLE

Crystal reorientation in methylammonium lead iodide perovskite thin film with thermal annealing

Shalinee Kavadiya^{a,b}, Joseph Strzalka^c, Dariusz M. Niedzwiedzki^d, and Pratim Biswas^{a,*}Received 00th January 20xx,
Accepted 00th January 20xx

DOI: 10.1039/x0xx00000x

While the progress in the performance of perovskite solar cells is rapidly evolving, the details of film formation, effect of processing parameters and perovskite crystal structure are still under discussion. The details of the XRD pattern of the tetragonal phase of $\text{CH}_3\text{NH}_3\text{PbI}_3$ perovskite existing at room temperature is often overlooked, with unresolved (002) (at $2\theta = 13.99^\circ$ for $\text{CuK}\alpha$ and $q = 0.9927 \text{ \AA}^{-1}$) and (110) (at $2\theta = 14.14^\circ$ and $q = 1.003 \text{ \AA}^{-1}$) peaks considered to be one peak at 14° , leading to an inaccurate estimation of lattice parameters. In this study, we use an electrospray deposition technique to prepare perovskite films at room temperature; oriented in (002) and (110), with (002) as the preferred orientation. The results of a detailed study on the emergence of the two orientations during perovskite formation are reported. The effect of process parameters, such as substrate temperature during deposition and annealing temperature, on the grain orientation was established using XRD and grazing incidence wide angle X-ray scattering (GIWAXS). The study suggests that an irreversible crystal reorientation from (002) to (110) occurs at high temperature during rapid annealing, whereas a reversible crystal thermal expansion is seen during slow annealing. Finally, the results of the grain reorientation are correlated with the film properties, and it is shown that the film with dominant (110) orientation has improved morphology and optoelectronic properties. The detailed structural investigation and characterization presented in this study is important for the precise determination of crystal orientation and achieving desirable photovoltaic properties of the absorber material by carefully observing the adjacent crystal plane peaks in the XRD pattern of the perovskite thin films.

Introduction

In a few years span, active research on organometallic halide perovskite solar cells has yielded the highest certified power conversion efficiency of 23.3%¹. The prototypical and most studied halide perovskite is methylammonium lead iodide ($\text{CH}_3\text{NH}_3\text{PbI}_3$, abbreviated as MAPbI₃) because of its easy and low-temperature fabrication, wide absorption range (band gap = 1.55 eV), high defect tolerance, and excellent electronic properties. A variety of techniques have been reported to deposit perovskite films, broadly categorized as, dip coating², spin-coating^{3,4}, ink-jet printing⁵, spray deposition⁶⁻⁹, and vapor-based deposition¹⁰, with the solution-based techniques being easy to perform and requiring low energy input. Commonly, most of the techniques necessitate annealing treatment (temperature between 80-150 °C) of the perovskite film after deposition to ensure complete evaporation of the solvent and crystallization of the perovskite material. Previous studies had

optimized annealing temperature and time, depending on the fabrication environment¹¹⁻¹⁴ for complete formation of perovskite. Moreover, various other annealing procedures and environments, namely, solvent vapor annealing¹⁵, air annealing¹⁶, photonic flash-annealing¹⁷, low-pressure vapor annealing¹⁸, and gas blowing¹⁹ have been introduced to obtain uniform coverage of the film with a smooth surface and large grain size, necessary for superior device performance. Thermal annealing is also known to promote degradation of perovskite by inducing strain in the film during thermal expansion and contraction during annealing and cooling²⁰. Therefore, methods for annealing-free/room temperature formation of perovskite have also been demonstrated through 1) rapid anti-solvent crystallization^{21,22} or solvent-solvent extraction²³; and 2) incorporation of an additive into the precursor solution^{24,25}. However, in some of these methods, post-annealing has shown further improvement in the film properties and device efficiency²¹⁻²³.

The effect of annealing is primarily observed on perovskite crystallization and morphology of the film. The crystal structure and grain size are analyzed using an X-ray diffractometer, focusing on relative change in intensity of the diffraction peaks of perovskite and lead iodide. However, the X-ray diffraction (XRD) pattern of perovskite has been overlooked, as in the peaks at $2\theta = 13.99^\circ$ and 14.14° , corresponding to (002) and (110) reflections^{26,27}, respectively, of the tetragonal perovskite phase (lattice dimension $a = b = 8.849 \text{ \AA}$, $c = 12.642 \text{ \AA}$); usually identified as one peak with (110) reflection, and the variation

^a Aerosol and Air Quality Research Laboratory, Department of Energy, Environmental and Chemical Engineering, Washington University in St. Louis, MO 63130, USA

^b School of Electrical, Computer, and Energy Engineering, Arizona State University (ASU), Tempe, Arizona 85287-5706, USA

^c X-ray Science Division, Argonne National Laboratory, Lemont, IL 60439 USA

^d Department of Energy, Environmental and Chemical Engineering, Center for Solar Energy and Energy Storage, Washington University in St. Louis, St. Louis 63130

Electronic Supplementary Information (ESI) available.

*Email - pbiswas@wustl.edu

between these peaks with annealing has often been ignored. Similarly, the other peaks are also not distinguished and identified, such as (004) and (220) peak at 28.2° and 28.5° are classified as (220). Additionally, all three phases of MAPbI₃ perovskite: orthogonal (exist at temperature $T < -103^\circ\text{C}$), tetragonal ($-103^\circ\text{C} < T < 57^\circ\text{C}$), and cubic ($T > 57^\circ\text{C}$) have peaks that are very close²⁷⁻²⁹. For example, (101) of the orthorhombic phase at 14.41° ; (002)/(110) of the tetragonal phase at $13.99^\circ/14.14^\circ$; and (001) of the cubic phase at 14.01° . This sometimes leads to a misinterpretation of the crystal structure. While this ambiguity in classifying the (002) and (110) as one (110) peak occurs mainly due to poor instrument resolution (close reflections cannot be resolved), the wide range plots of 2θ scan exacerbates this by the inability to distinguish the two adjacent peaks. However, such an approximation leads to inaccuracy in the calculation of the lattice parameters and determination of the crystal structure, and misguides in relating the structural characteristic to the film properties.

For a detailed understanding of the structural-property relationship of the perovskite film, it is very important to precisely classify the crystal structure and investigate its effect on the optoelectronic properties of the film. A few studies have elucidated the existence of these pairs of peaks ((002) & (110) and (004) & (220)) and their relative variation as a function of the process parameters³⁰⁻³³. Docampo et al. discussed the dependency of the orientation of MAPbI₃ on the temperature of methylammonium iodide (MAI) solution during dip coating on PbI₂ substrates, and reported that the crystal orientation changes from (002) to (110) with an increase of temperature³². A large portion of (110)-oriented crystals appears at higher temperatures as the (002)-oriented crystals disappear above a specific temperature. Additionally, an increase in short-circuit current for the (110)-oriented crystals was observed, probably resulting from anisotropic electronic properties of the perovskite. Another study by Lilliu et al.³³ focused on the importance of resolving the pair of close peaks in perovskite XRD and their effect on power conversion efficiency. The authors used scanning nanofocus XRD in transmission geometry to probe the local variation in the orientation of individual grain

and found the presence of both (002)- and (110)-oriented grains. The study also reports variation in the orientation as a function of substrate temperature during one-step spin coating of perovskite precursors. The perovskite grain size was found to increase with temperature (up to 90°C) along with the presence of grains oriented in [110] direction. A significant amount of grains oriented in [002] direction were still found in the film spun at 90°C . Yet another study was able to resolve (004) and (220) peaks and found that (004) orientation is preferred at high PbI₂ to MAI flux through the vapor deposition of the perovskite³¹. Therefore, it is vital to perform a detailed structural analysis of the perovskite, examine the emergence of the two close XRD peaks as a function of time during perovskite formation, and their variation with process parameters, which could be associated with the optoelectronic properties of the perovskite.

Previously, we have successfully demonstrated an electro-spray deposition technique to fabricate MAPbI₃ perovskite layer for stable perovskite solar cells under ambient humidity (30-50% relative humidity)⁸. The method follows two steps: PbI₂ is first deposited by spin coating, and then, MAI is electro-sprayed on the PbI₂ layer. In the electro-spray process, charged MAI droplets are generated and directed towards the PbI₂-coated substrate, connected to ground. The solvent evaporates before the arrival of droplets on the substrate, and charged MAI particles react with PbI₂ and form perovskite film. The as-deposited, tetragonal-phase perovskite film consists of grains oriented in [002] and [110] directions with [002] as the preferred orientation. However, annealing the film reorients the grain in [002] direction to [110] direction and merges with grains orientated in [110]. Therefore, this technique is useful to execute a detailed investigation on the presence of two orientations under different processing conditions, control the crystal-structure, and inspect the effect of orientation on properties of perovskite film.

In this work, we employ the electro-spray technique to deposit perovskite layers and systematically investigate the occurrence of the different crystal orientations and their effect on film properties. First, we study the emergence of the two

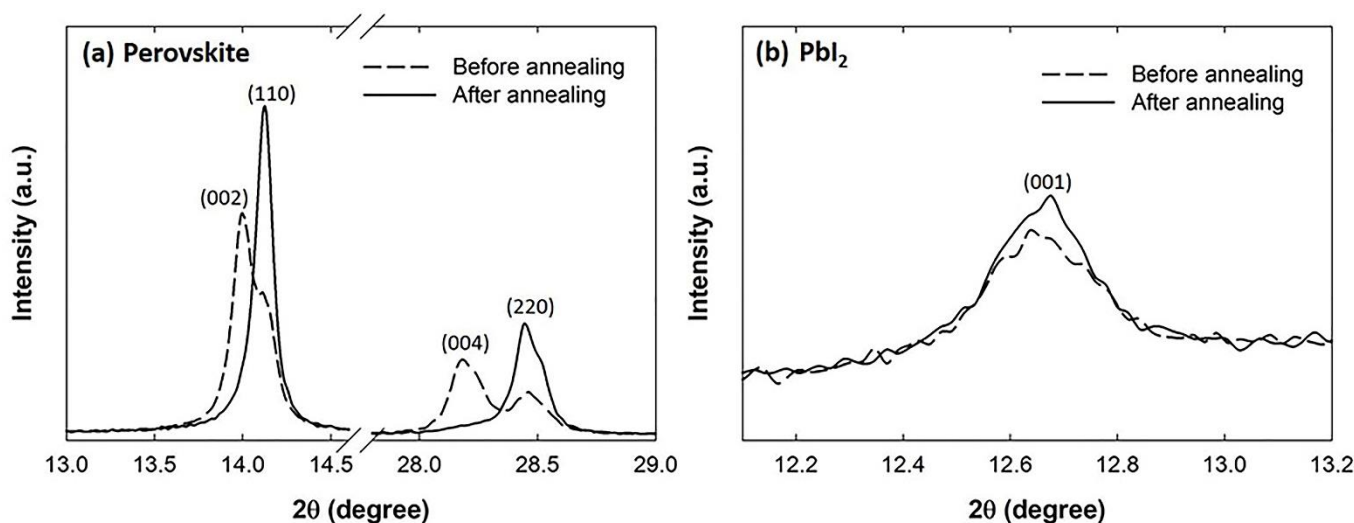


Figure 1. XRD pattern of the electro-sprayed perovskite film taken before (dashed curve) and after annealing (solid curve) at 100°C for 5 min showing (a) perovskite peaks with clear difference between (002) & (110) and (004) & (220) peaks and (b) PbI₂ (001) peaks. Note that the y-axis in (b) is expanded 11x to that of y-axis in (a).

orientations during the perovskite formation at different temperatures. Second, the change in crystal orientation of the deposited perovskite film as a function of annealing temperature is determined. Third, we investigate the effect of annealing procedure (rapid and slow annealing) on the crystal orientation. Finally, we study the effect on morphological, optical, and electronic properties of perovskite. These detailed structural investigations help deepen the general understanding of perovskite film growth as well as structure and temperature related stability issues.

Results and discussion

Crystal reorientation during annealing

A polycrystalline perovskite film was deposited in two steps: first, PbI_2 was deposited using spin coating, then MAI using electro spray (experimental details are provided in the supporting information (SI)). For electro spray deposition, a solution of MAI in IPA (14 mg/ml) was pumped at a flow rate of 1 μLPM through a needle connected to a high voltage source. Monodisperse charged droplets containing MAI are generated in Taylor cone-jet mode, which then travel in the electric field towards the grounded PbI_2 -coated substrate. The charged MAI particles reach the substrate, react with PbI_2 and form the perovskite. Figure 1a, dashed curve shows the XRD of the as-deposited (before annealing) perovskite film, showing the vztetragonal phase as manifested by splitting of the characteristic diffractive peaks; a major peak at 13.99° corresponding to (002) plane and a minor peak/shoulder at 14.14° , corresponding to (110) plane. The preferred orientation of grains at room temperature is with the [002] direction normal to the substrate surface because of the underlying mechanism of PbI_2 to perovskite conversion. Similar to vapor phase formation of perovskite, in the electro spray-assisted fabrication, the formation occurs by diffusion-intercalation of MAI into the layered PbI_2 structure, because MAI is supplied in the form of nanoparticles at a gradual rate, contrary to the spin coating method where MAI solution is supplied in bulk and the reaction mechanism depends on the MAI concentration³⁴. Intercalation of MAI causes twisting of corner sharing PbI_6 octahedron in the layered structure of PbI_2 and forms Pb-I bonds between the PbI_2 layers, resulting in 3D perovskite structure oriented along the [002] direction. Previous studies reported strongly preferred orientation along [002] direction, in the case of vapor reacted perovskite crystals, but of cubic phase because the reaction was performed at high temperature³⁵. However, in this study, the reaction occurs at room temperature and therefore, the (002) peak seen is that of the tetragonal perovskite. Additionally, a clear splitting to two peaks at $\sim 14^\circ$ confirms them as being (002) and (110) peaks of the tetragonal perovskite. The high index peaks of these families, (004) at 28.21° and (220) at 28.5° , are low in intensity but easy to distinguish because of the large 2θ difference between them. Figure 1b shows the same XRD as in Figure 1a but zoomed in on the tiny PbI_2 peak, coming from either some

unreacted fraction or area on the substrate covered with a clamp during electro spray of MAI.

After taking the XRD measurements, the films were annealed rapidly at 100°C for 5 min. The solid curve in Figure 1 is the XRD pattern of the same film after annealing and shows that the (002) and (004) peaks disappear almost completely, whereas the (110) and (220) peaks amplified. The change in the relative intensity of the perovskite peaks suggests that the grains oriented along [002] direction change their orientation to [110] and merge with the grains orientated along [110] direction, which also denotes that the grain size will increase after annealing (discussed in the later section). The PbI_2 peak in Figure 1b does not show any shift with annealing; which verifies that the change in the perovskite peaks does not arise from any measurement error. The complete XRD plots from $2\theta = 5$ to 40° of the same film before and after annealing are presented in Figure S1a. Similar change in the intensity is also observed in other orientations of perovskite present in very small fraction, where (112) and (114) peaks diminish and their nearby peaks (200) and (222) amplify respectively (SI, Figure S1 b and c).

It is important to further validate that the origin of the alteration in peak intensities is associated with the crystal reorientation (change in the population of the grains oriented in [002] and [110] directions) by considering other possibilities, such as (1) excess MAI electro sprayed, and (2) perovskite phase transition. Electro spraying of excess MAI may lead to the presence of excess MA^+ and/or I^- in the crystal structure, which then evaporates during annealing, resulting in crystal shrinkage and rightward shift of the XRD peaks. To check this possibility, we fabricated other types of perovskites, such as methylammonium lead iodide-bromide ($\text{MAPbI}_{3-x}\text{Br}_x$), methylammonium lead iodide-chloride ($\text{MAPbI}_{3-x}\text{Cl}_x$) and formamidinium lead iodide (FAPbI_3). All the three perovskites were fabricated by spin coating the PbI_2 layer and electro spraying MABr, MAI and FAI in the same amount as electro spray of MAI, to form $\text{MAPbI}_{3-x}\text{Br}_x$, $\text{MAPbI}_{3-x}\text{Cl}_x$, and FAPbI_3 , respectively. Electro spraying MABr on PbI_2 forms a mixed iodide-bromide perovskite, $\text{MAPbI}_{3-x}\text{Br}_x$ (Figure S2a) and shows no change in the position of the perovskite XRD peaks after annealing. Electro spraying MAI on PbI_2 forms segregated MAPbI_3 and MAPbCl_3 phases as shown in the Figure S2b because of the low solubility of chloride ion in iodide-based perovskite. The XRD pattern clearly indicates a change in position of the MAPbI_3 XRD peaks (at $\sim 14^\circ$ and 28°), but no such transformation for MAPbCl_3 . Similarly, no change is observed in the case of FAPbI_3 (Figure S2c) as well. Considering the fabrication of different types of perovskites, the peak position change is only observed in the case of MAPbI_3 , supporting the presence of both the (002) and (110) families of XRD peaks before annealing, corresponding to the tetragonal structure of MAPbI_3 , in which (002) orientation changes to (110) during annealing. If the change in crystal structure is because of the excess electro spraying of AX ($\text{A} = \text{MA}^+/\text{FA}^+$ and $\text{X} = \text{I}^-/\text{Br}^-/\text{Cl}^-$), it would be visible in the case of other perovskites as well. Moreover, intentional electro spraying of excess MAI results in the presence of isolated MAI in the film, giving rise to the diffraction peaks from MAI crystals at 9.6° , 19.6° , and 29.6° ⁸.

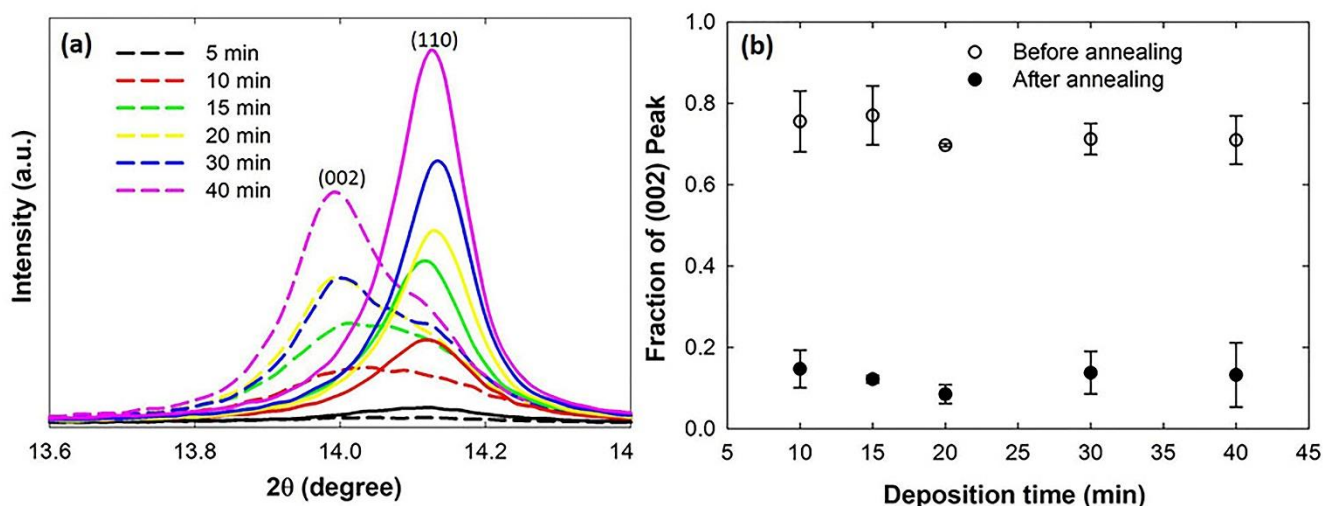


Figure 2 (a) XRD pattern of the perovskite film prepared at different electro spray deposition times and taken before (dashed curve) and after annealing (solid curve) at 100 °C for 5 min. (b) Fraction of (002) peak in the total perovskite peak at 14° ((002)+(110) peaks) as a function of deposition time before (hollow circle) and after annealing (filled circle).

MAPbI₃ undergoes a phase transition from tetragonal to cubic structure at 57 °C. However, the results suggest a change in relative intensity of (002) and (110) peaks, no simultaneous shift in both (110) and (002) reflections to merge together at 14.01° (corresponding to the (001) peak of cubic perovskite^{26, 27}) is observed, which eliminates the possibility that the change in the XRD peaks is related to phase transition of perovskite. Additionally, the presence of (211) reflection position at 2θ = 23.5° (Figure S1b), which is inconsistent with the cubic symmetry of MAPbI₃, also supports the hypothesis that the change in the peaks is not related to the phase transition of MAPbI₃.

Emergence of the two orientations

After resolving close peaks in the XRD pattern and observing the change in crystal orientation by annealing, the emergence of the two families of peaks and their variation with annealing was studied. For this analysis, we deconvoluted the peaks and calculated the area under each of them to represent the amount of grain orientated into each direction. Since the peaks ((002) and (110)) at ~ 14° have the highest intensity, they were used for further analysis in this work. Curve fitting was performed in the range 2θ = 13.6 to 14.4° on a background subtracted XRD using a Voigt function (combination of Gaussian and Lorentzian), which mimics shapes of both peaks (peak 1 at 13.99° and peak 2 at 14.14°). Peak positions were kept constant during fitting. The detailed curve fitting results are shown in Figure S3, corresponding to the before and after annealing XRD pattern displayed in Figure 1. The Voigt function fits the XRD well with R² > 0.99 for all the cases. After fitting the two peaks, the fractions of each peak ($F_{(002) \text{ or } (110)}$) is calculated by:

$$F_{(002) \text{ or } (110)} = \frac{\text{Area of (002) or (110) peak}}{\text{Area of (002) peak} + \text{Area of (110) peak}} \quad (1)$$

Figure 2a shows the XRD of the perovskite film deposited for different MAI electro spray time before annealing (dashed curve) and after annealing (solid curve), indicating the evolution of (002) and (110) peaks as the perovskite formation occurs. As the electro spray deposition time increases, perovskite peak intensity increases because of the reaction between MAI and

PbI₂, and the formation of perovskite. We can see that both peaks emerge and grow together, however, (002) peak grows at a higher rate and therefore has higher intensity than the (110) peak before annealing. Interestingly, the total fraction of (002) peak in the convoluted (002) and (110) peaks, calculated by equation 1, remains almost constant in the range 0.7-0.8 as the deposition time increases (Figure 2b). After annealing the films, the (002) peak diminishes, and XRD of all the films are aligned at (110) reflection (solid curves in Figure 2a). The total fraction of (002) peak reduces to 0.15-0.05 for all the deposition time. The corresponding XRD patterns focused on PbI₂ peak (12.6°) and (211) peak of perovskite for different deposition time are shown in Figure S4a and S4b, respectively, showing no displacement in these peaks with annealing. Additionally, (211) reflection position at 2θ = 23.5°, which is consistent with tetragonal perovskite but inconsistent with the higher-temperature cubic phase, was also observed after annealing (Figure S4b).

Effect of substrate and annealing temperatures

The process of annealing is very crucial and has been shown to significantly influence the film crystallinity. The effect of substrate temperature during deposition and annealing temperature on the crystal orientation was studied. The temperature at which reorientation occurs and the (110) orientation is favored during the perovskite formation was determined. This was done by preparing perovskite samples at different temperatures by electro spraying MAI on the PbI₂-coated substrates held at different temperatures ranging from 25 °C to 55 °C. Figure 3a displays their XRD pattern before (dashed curve) and after annealing (solid curve). The (002) orientation is preferred at room temperature, whereas upon increasing the substrate temperature, the (110) peak starts to rise and becomes dominant. Figure 3b shows the fractional area of (002) and (110) reflections before and after annealing as a function of substrate temperature. The fraction of the (110) peak area increases, as the (002) peak area decreases upon increase of substrate temperature. The increase in the fraction of the (110) peak with substrate temperature compared to its

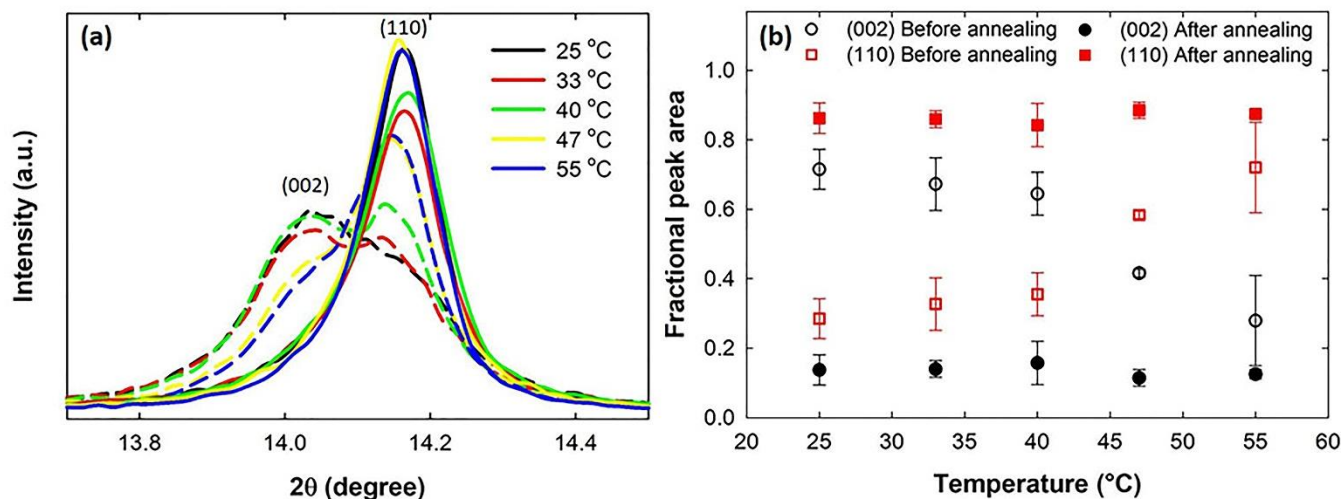


Figure 3 (a) XRD pattern of the perovskite film prepared at different substrate temperatures during electro-spray deposition and taken before (dashed curve) and after annealing (solid curve). (b) Fraction of XRD peak area of the perovskite peak (002) (circles) and (110) (squares) before (hollow symbols) and after annealing (filled symbols) as a function of substrate temperature.

fraction in the film deposited at room temperature at all the deposition times is observed. This occurs as at higher substrate temperatures, the perovskite grains oriented in the (002) during deposition transform to the (110) orientation. Overall, grains are first oriented in (002) during deposition and then convert to (110) orientation with time as more energy is provided at high substrate temperature. Consequently, the conversion from (002) to (110) is higher at higher substrate temperatures. This is also consistent with Lilliu et al.³³, which described the dominance of (110) orientation rather than (002) at a high substrate temperatures during spin coating of perovskite precursors. The substrate temperatures used in their study³³ were much higher than in the present study because of direct solution deposition, requiring additional energy (heat) to evaporate the solvent and then form the perovskite. At ~ 43 °C substrate temperature, (110) orientation begins to dominate in the as-deposited perovskite film. Beyond 43 °C, perovskite oriented in [110] direction dominates and at 55 °C, the average fraction of (110) peak is similar to that of the fraction of (002) peak in the film fabricated at room temperature, exactly inverting the orientation composition. At high temperatures, the film looked rough and hazy, which is due to faster reaction

between MAI and PbI_2 compared to electro-spray deposition at room temperature, similar to previously reported on two-step deposition of perovskite^{6, 36, 37}. At very high temperatures (above 55 °C) electro-spray of MAI does not even adhere to the film because of its high volatility, and hence those temperatures are not considered here. These films were then annealed at 100 °C for 5 min, and the XRD patterns of all films aligned at (110) peak. Further enhancement in the fraction of (110) peak was observed (filled symbols) because of the conversion of remaining grains oriented in (002) to (110) orientation with annealing. Overall, the fraction of (002) peak reduces, and that of (110) peak enhances in the annealed film. Interestingly, the total fraction of (110) peak in all the annealed film for all the substrate temperatures is constant, ~ 0.85, irrespective of the (002) peak fraction present before annealing. This suggests that the transformation/grain reorientation is kinetically very fast at 100 °C, however, still a small amount (< 15%) of (002) oriented grains are always retained in the film after annealing. In order to determine the temperature at which reorientation occurs and calculate the activation energy for reorientation from (002) to (110), the films were synthesized at room temperature, with the dominating (002) orientation, and

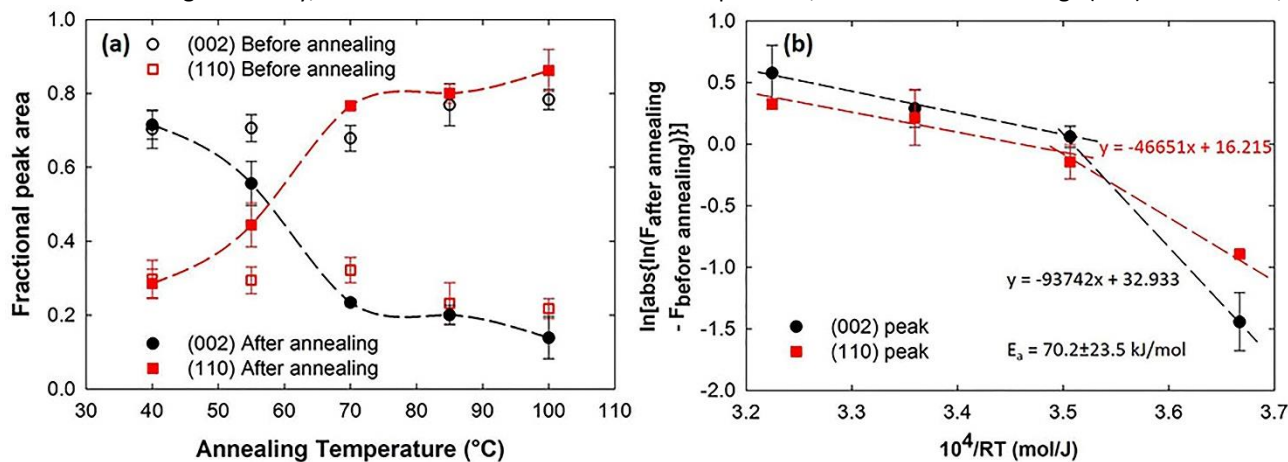


Figure 4 (a) Fraction of (002) (circles) and (110) (squares) peak area before and after annealing, and (b) Fractional change in the peak area of (002) and (110) peaks with annealing as a function of annealing temperature.

annealed at various temperatures for 5 minutes. The synthesized films contain 75-80% fraction of perovskite grains orientated in [002] direction and 25% in [110] direction (open symbols in Figure 4a), similar to Figure 2b and Figure 3b. Annealing at 40 °C does not affect the crystal orientation significantly, however, as the temperature increases, grains reorient from [002] to [110] directions and fraction of (110) peak increases. Higher annealing temperature increases the conversion from (002) to (110) orientation, and the conversion occurs at ~ 58 °C. However, at certain temperatures (around 85 °C and beyond), reorientation is very fast and the fraction of each orientation saturates. The highest fraction of perovskite oriented in [110] direction reaches around 70% after annealing at 100 °C, and annealing the films at temperature > 100 °C does not significantly change the crystallinity, but can destroy the film morphology by forming large islands, and degrade perovskite, as reported previously¹². There is still some amount of grains oriented in [002] direction present in the film after annealing at 100 °C, which might be because of the close proximity of the two peaks, making it difficult to completely eliminate the (002) peak from the tail of (110) peak. The activation energy of reorientation is calculated by solving the first order rate of change in fractional peak area (F) of the two peaks:

$$\frac{d[F]}{dt} = \pm A_0 \exp\left(\frac{-E_a}{R \cdot T}\right) [F] \quad (2)$$

Where A_0 is a pre-factor, E_a is the activation energy, - sign is for (002) peak as it decreases with annealing, and + sign is for (110) peak as it increases with annealing. Initial conditions are: at $t = 0$, $F =$ fractional area before annealing ($F_{\text{before annealing}}$), and at $t = t_f$, $F =$ fractional area after annealing ($F_{\text{after annealing}}$). Solving the equation 2 gives:

$$\ln(F_{\text{after annealing}}) - \ln(F_{\text{before annealing}}) = \pm A_0 t_f \exp\left(\frac{-E_a}{R \cdot T}\right) \quad (3)$$

The plots of natural log of left hand side as function of $1/R \cdot T$ for both the (002) and (110) peaks are shown in Figure 4b, further indicating that the process is very fast at higher temperatures so the change in the peak area saturates at certain temperature. Therefore, the activation energy is calculated by the average of

the slope of the curves at low temperature ($10^4/R \cdot T > 3.45$ mol/J) and is (70.2 ± 23.5) kJ/mol. To our best knowledge, this is the first estimation of the activation energy for such grain reorientation in MAPbI₃ films. Nonetheless, the trend in the change in the orientation with temperature matches the previous study^{32, 33}.

Effect of annealing procedure: rapid vs. slow annealing

In order to capture transformation during annealing, an *in-situ* XRD measurement would be desirable, but the time required for a theta-theta scan is not compatible with the fast kinetics of the process. Some groups have successfully reported time-resolved XRD measurements³⁸⁻⁴¹, but these are generally not routinely available. Instead, we applied grazing incidence wide angle x-ray scattering technique, more compatible with *in-situ* measurements. GIWAXS provides a 2D scattering plot of intensity as a function of photon wave vector transfer (q) was obtained at each measurement. In grazing-incidence geometry, the components of the scattering vector q are given by

$$q_x = \frac{2\pi}{\lambda} (\cos \alpha_f \cos 2\theta_f - \cos \alpha_i) \quad (4a)$$

$$q_y = \frac{2\pi}{\lambda} \cos \alpha_f \sin 2\theta_f \quad (4b)$$

$$q_z = \frac{2\pi}{\lambda} (\sin \alpha_i + \sin \alpha_f) \quad (4c)$$

For the specular reflection condition maintained in our XRD theta-theta scans, $\alpha_i = \alpha_f = \theta$, the photon wave vector transfer is all in the z-direction and becomes:

$$q = \frac{4\pi}{\lambda} \sin \theta = \frac{2\pi}{d} \quad (5)$$

Where d is the spacing between the crystal planes. Therefore, $2\theta = 13.99$ and 14.14° representing (002) and (110) plane, corresponds to $q = 0.9927$ and 1.0033 \AA^{-1} , for Cu K α wavelength used in XRD. Figure 5a shows 2D GIWAXS pattern of perovskite prepared on TiO₂/FTO slide before annealing, exhibiting crystalline domains orientated in [002] and [110] direction out-of-plane. The azimuthally integrated scattering intensity (azimuthal angle ranging from 90° to 180° , corresponding to the top-left quadrant of the GIWAXS pattern) is plotted in Figure S5 (SI) as a function of scattering vector, q , over the

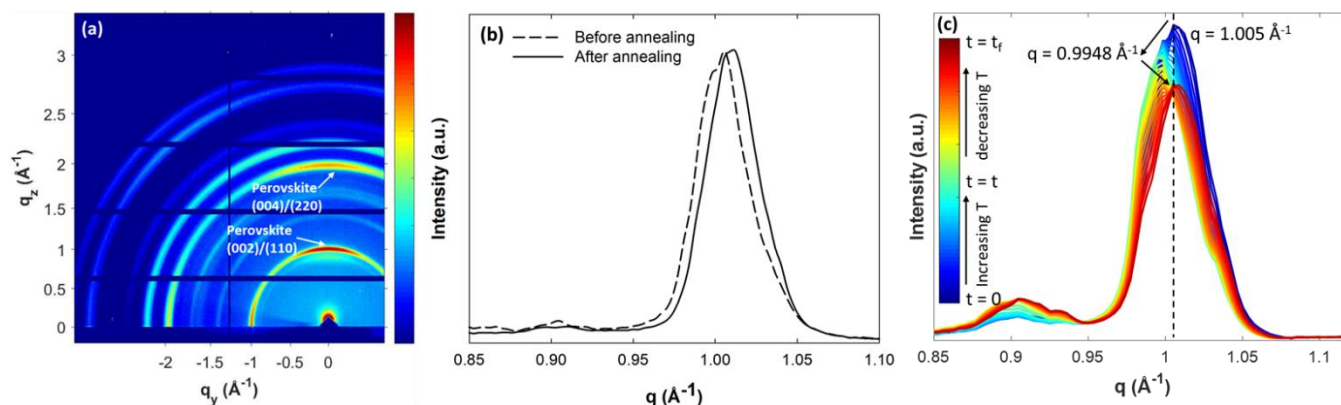


Figure 5(a) 2D GIWAXS pattern of the perovskite film deposited on the TiO₂/FTO slide before annealing. (b) Azimuthally integrated intensity of GIWAXS pattern as a function of scattering wave vector at different temperatures (T) during slow annealing, including temperature increase (from $t = 0$ to t , $T = 30^\circ\text{C}$ to 100°C) and decrease period (from $t = t_f$ to t , $T = 100^\circ\text{C}$ to $T = 30^\circ\text{C}$). (c) Azimuthally integrated intensity vs scattering wave vector for rapid-annealed films before (dashed curve) and after (solid curve) annealing.

range of q that includes the perovskite (002) and (110) features. A broad peak of perovskite is observed in the q range of $0.9635\text{--}1.061\text{ \AA}^{-1}$, consistent with the experimental resolution, which in this q -range is about 0.05 \AA^{-1} , dominated by the geometry of the measurement⁴². The highest peak intensity at $q = 1.005\text{ \AA}^{-1}$, contrary to the expected peak at 0.9927 \AA^{-1} . A small rightward shift of the peak position might come from the small experimental error of the distance between the sample and the detector. Additionally, we could not observe a clear difference between the (002) and (110) XRD peaks. However, a trend on the peak shift could still be observed allowing investigate change in the crystal orientation as a function of the annealing temperature. The film was first annealed for 5 min on the $100\text{ }^\circ\text{C}$ hot plate and quickly quenched. Figure 5b shows azimuthally integrated scattered intensity before and after annealing and indicate a rightward shift of the peak, compatible with the observation from XRD. Then, *in-situ* GIWAXS was performed to investigate the change during annealing. The sample was kept on a thermal stage, the temperature was increased at a rate of $20\text{ }^\circ\text{C}/\text{min}$ up to $100\text{ }^\circ\text{C}$ and then decreased to room temperature, and measurements were taken at every $5\text{ }^\circ\text{C}$ change. Azimuthally integrated intensity profiles of the GIWAXS pattern taken at various temperatures during warming up from $30\text{ }^\circ\text{C}$ to $100\text{ }^\circ\text{C}$ and cooling down to $30\text{ }^\circ\text{C}$ are displayed together in Figure 5c. Important to note that a correction due to the thermal expansion of the sample and stage was taken by realigning the sample at each temperature as mentioned in the experimental section. Interestingly, the perovskite peak shifts leftward during temperature increment, shifts back rightward as temperature decreases, and returns to the original

position. This kind of shift is usually because of the thermal expansion and contraction of the material during increase and decrease of temperature, respectively²⁰. Moreover, the peak intensity decreases, which may be due to the degradation as a slight increase in corresponding lead iodide peak is also observed. The observed peak shift during annealing is contrary to the observation from rapid annealing for 5 min, where a rightward shift of (002) to (110) peak occurs. This dissimilarity occurs from different annealing procedure used during the measurements. When the films were annealed slowly while the measurements were taken, thermal expansion and contraction of material was observed. Overall, crystalline perovskite film is formed during electrospray deposition at room temperature, which then exhibits crystal structure change in different annealing environments. In rapid annealing and quenching, orientation of grains changes from [002] direction to [110] (rightward to [002]) irreversibly, whereas, during slow annealing, a reversible leftward peak shift occurs due to temporal thermal expansion of the perovskite. Additionally, the reversible peak shift during slow annealing is also observed for the case of mixed halide perovskite ($\text{MAPbI}_{3-x}\text{Br}_x$) (Figure S6, SI), which does not have phase transition in this range of temperature, and further confirms that the origin is the thermal expansion.

Effect of change in crystal orientation on perovskite film properties

The power conversion efficiency of perovskite solar cells strongly depends on the film morphology and its electronic and optical properties. Therefore, it is vital to investigate the effect of the

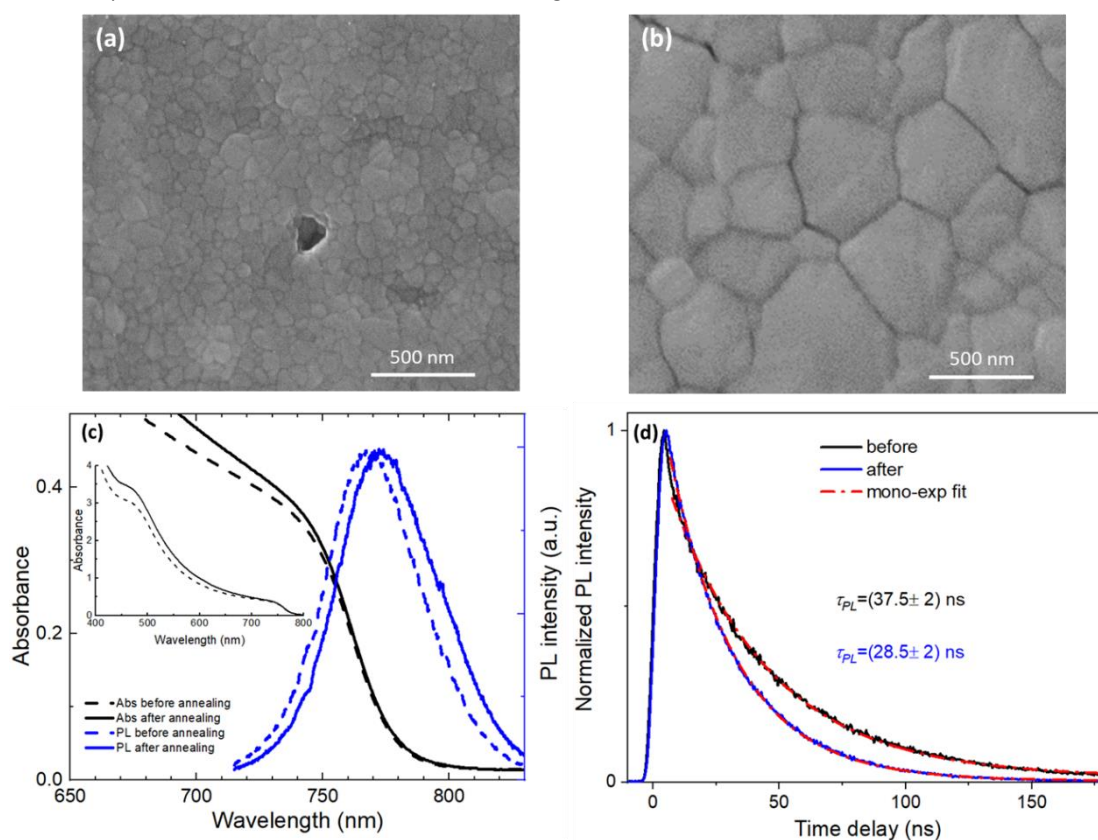


Figure 6 SEM images of the perovskite film deposited on the TiO_2/FTO substrate taken (a) before and (b) after annealing at $100\text{ }^\circ\text{C}$ for 5 min. (c) Steady-state absorption and photoluminescence spectra before (dashed curve) and after (solid curve) annealing. (d) Time-resolved photoluminescence before and after annealing. The decay curves were fit with monoexponential decay function ignoring instrument response function of the spectrometer. The photoluminescence decay lifetime (τ_{PL}) represents average value from measurements of two different samples.

change in the crystal orientation on the film properties. Additionally, previous studies showed anisotropy in the properties of perovskite, which change with their crystal orientation: for example, *anisotropy in charge transport* of orientationally pure crystalline MAPbI₃ perovskite film fabricated using a thermal-gradient-assisted directional crystallization⁴³, *anisotropy in mechanical properties* (bulk, shear, and Young's modulus)⁴⁴, and *absorption properties*. The film morphology was characterized by scanning electron microscopy, optical properties by its absorption and photoluminescence spectra, and charge transport properties by time-resolved photoluminescence measurements of the films before and after 5 min annealing at 100 °C. SEM images of the perovskite film deposited on TiO₂/FTO substrate before and after annealing (Figure 6a, b) indicate that annealing increases the grain size, heals any pin holes present in the film, and improves film smoothness. The grain size increases from 76 ± 2 nm before annealing to 320 ± 11 nm after annealing (calculated from the SEM images). Annealing-induced improvement in surface morphology/smoothness is well known in literature due to increase in the grain size. However, in this work increase in the grain size is the result of the conversion of crystal orientated in [002] direction to [110] direction and merging with crystals oriented in [110] direction. This is further sustained by the decrease in the full width half maxima of the (110) peak in the XRD pattern with annealing and the fact that the total peak area (sum of (002) and (110) peak areas) remains nearly the same before and after annealing. Change in the surface morphology suggest that annealing is beneficial to obtain good quality film.

Annealing-mediated improvement in morphology of the perovskite layer affects also luminescence properties of the perovskite film. Figure 6c shows steady-state absorption and photoluminescence (PL) spectra of the MAPbI₃ perovskite film deposited on TiO₂/FTO substrate before and after annealing. The PL spectra represent time-integrated spectra of time-resolved PL measured to characterize dynamics of PL decay. The PL spectra are normalized to their maxima for better comparison. Note that as the position of the inter-band absorption essentially does not change after annealing, though probably the absorption coefficient does, resulting in the higher absorbance level, and an apparent shift toward longer wavelengths is observed for PL emission. The spectrum shifts from 767 to 773 nm, corresponding to ~10 meV energetic shift toward lower energies. The PL emission is associated with a radiative recombination of photogenerated charges but may have various origins including band-to-band transition (free charge recombination) and exciton recombination. Recently it was argued that for the organolead trihalide perovskites at low excitation intensities, comparable to working condition of the solar cell, PL occurs mostly from recombination of excitons weakly localized just below energetic mobility edge, a working regime of the solar cell. It may be surprising as the lack of band filling with free charges should prevent any photovoltaic application; however, at room temperature, those weakly localized excitons can be thermally activated, diffuse and "escape" above mobility edge and play role of free charge carriers⁴⁵. Spectral shift of the PL spectrum toward lower energies may be another confirmation that upon applied excitation intensity, PL indeed origins from recombination of weakly localized excitons. It is possible that the annealing process forms deeper local

minima in conduction band of MAPbI₃ (alternatively, local maxima in valence band, or both) to which excitons will relax to minimize their energy and then, after full relaxation, recombine/luminesce. Figure 6d shows dynamic characteristics of PL process of the MAPbI₃ perovskite film before and after annealing. In both cases, the decay curve could be successfully fitted with monoexponential decay, however the fitting gives vastly different PL decay lifetimes (τ_{PL}): 37.5 ns and 28.5 ns for sample before and after annealing, respectively. At first, it may be surprising as it was demonstrated that annealing greatly improves quality of perovskite film (notably its grain size is significantly increased, Figure 6a, b) and in consequence PL lifetime should rather increase, simple because expected mitigation of defect assisted non-radiative recombination on the grain surface.^{46, 47} However as it is true for a standalone perovskite film it may not be correct for the MAPbI₃/TiO₂/FTO device. Very likely annealing also improves the quenching properties of TiO₂ layer in the way that it leads to a better MAPbI₃/TiO₂ interface morphology and consequently enhanced charge carrier injection from the MAPbI₃ film to TiO₂ layer. It is actually desirable, it should improve photovoltaic performance of the device. Therefore, on one hand, annealing should elongate PL lifetime of the MAPbI₃ film, but on the other hand the rate of extraction free charge from a conduction band of the MAPbI₃ to TiO₂ becomes greater and may easily overcome the first effect. As a result, shortening not elongating of the PL lifetime could be observed as well, specifically as it occurs in the annealed sample.

One drawback of our fabrication method is that we cannot synthesize perovskite crystals fully oriented in only (002) direction, to investigate the properties of grains in (002) orientation, which would be interesting to compare. In our method, both (002) and (110) emerge together during the formation of perovskite, while the former develops at a higher rate. Overall, the difference in the properties before and after annealing suggest that it is critical to evaluate XRD close peaks and reach full conversion to perovskite oriented in (110) direction in order to achieve desired structural and optoelectronic properties of the film for maximum power conversion efficiency, and for precise determination of lattice parameters. Maximum orientation conversion to (110) can be achieved by thermal treatment as described in the present study, or by changing the perovskite precursor ratio³¹.

Conclusions

The formation of the perovskite film oriented in (002) and (110) directions was elucidated in this study. The perovskite films were deposited using an electrospray technique, and the emergence of the two orientations was studied during perovskite formation. Additionally, the effect of process parameters, substrate temperature, and post-annealing temperature on grain orientation and subsequently on the film properties was investigated. Two types of annealing, rapid and slow, were studied with *in-situ* measurements. The grains oriented in the [002] direction convert to the [110] direction at high temperature and merge with other grains with the (110) orientation irreversibly during rapid annealing at 100 °C for 5 min and rapid quenching. Whereas, during slow annealing and

cooling of the film, reversible thermal expansion and contraction in the crystal structure is observed. Importantly, films with (110) dominant orientation show enhanced light absorption, smooth morphology, and efficient charge carrier transport properties, which are desirable in photovoltaic devices. Therefore, the study shows the importance of closely resolving the XRD peaks of the deposited perovskite film.

Conflicts of interest

“There are no conflicts to declare”.

Acknowledgements

The work was supported by a grant from the National Science Foundation DMR 1806147, “Rational design of high-performance semiconductors based on inorganic properties”. This research used resources of the Advanced Photon Source, a U.S. Department of Energy (DOE) Office of Science User Facility operated for the DOE Office of Science by Argonne National Laboratory under Contract No. DE-AC02-06CH11357.

References

1. NREL, *National Renewable Energy Laboratory* http://www.nrel.gov/ncpv/images/efficiency_chart.jpg.
2. J. Burschka, N. Pellet, S.-J. Moon, R. Humphry-Baker, P. Gao, M. K. Nazeeruddin and M. Grätzel, *Nature*, 2013, **499**, 316-319.
3. J.-H. Im, H.-S. Kim and N.-G. Park, *Apl Materials*, 2014, **2**, 081510.
4. B. A. de Carvalho, S. Kavadiya, S. Huang, D. M. Niedzwiedzki and P. Biswas, *IEEE Journal of Photovoltaics*, 2017, **7**, 532-538.
5. Z. Wei, H. Chen, K. Yan and S. Yang, *Angewandte Chemie*, 2014, **126**, 13455-13459.
6. A. T. Barrows, A. J. Pearson, C. K. Kwak, A. D. Dunbar, A. R. Buckley and D. G. Lidzey, *Energy & Environmental Science*, 2014, **7**, 2944-2950.
7. M. Ramesh, K. M. Boopathi, T.-Y. Huang, Y.-C. Huang, C.-S. Tsao and C.-W. Chu, *ACS Applied Materials & Interfaces*, 2015, **7**, 2359-2366.
8. S. Kavadiya, D. M. Niedzwiedzki, S. Huang and P. Biswas, *Advanced Energy Materials*, 2017, DOI: 10.1002/aenm.201700210, 1700210.
9. S. Kavadiya, B. A. De Carvalho, S. Huang and P. Biswas, 2016.
10. M. Liu, M. B. Johnston and H. J. Snaith, *Nature*, 2013, **501**, 395-398.
11. T. Su, X. Li, Y. Zhang, F. Zhang and Z. Sheng, *Physical Chemistry Chemical Physics*, 2017, **19**, 13147-13152.
12. A. Dualeh, N. Tétreault, T. Moehl, P. Gao, M. K. Nazeeruddin and M. Grätzel, *Advanced Functional Materials*, 2014, **24**, 3250-3258.
13. Y. Li, L. Meng, Y. M. Yang, G. Xu, Z. Hong, Q. Chen, J. You, G. Li, Y. Yang and Y. Li, *Nature Communications*, 2016, **7**.
14. C. Zhang, Y. Luo, X. Chen, Y. Chen, Z. Sun and S. Huang, *Nano-Micro Letters*, 2016, **8**, 347-357.
15. J. Lian, Q. Wang, Y. Yuan, Y. Shao and J. Huang, *Journal of Materials Chemistry A*, 2015, **3**, 9146-9151.
16. S. R. Raga, M.-C. Jung, M. V. Lee, M. R. Leyden, Y. Kato and Y. Qi, *Chemistry of Materials*, 2015, **27**, 1597-1603.
17. J. Troughton, M. J. Carnie, M. L. Davies, C. Charbonneau, E. H. Jewell, D. A. Worsley and T. M. Watson, *Journal of Materials Chemistry A*, 2016, **4**, 3471-3476.
18. Y. Li, J. K. Cooper, R. Buonsanti, C. Giannini, Y. Liu, F. M. Toma and I. D. Sharp, *The Journal of Physical Chemistry Letters*, 2015, **6**, 493-499.
19. F. Huang, Y. Dkhissi, W. Huang, M. Xiao, I. Benesperi, S. Rubanov, Y. Zhu, X. Lin, L. Jiang and Y. Zhou, *Nano Energy*, 2014, **10**, 10-18.
20. J. Zhao, Y. Deng, H. Wei, X. Zheng, Z. Yu, Y. Shao, J. E. Shield and J. Huang, *Science Advances*, 2017, **3**, eaao5616.
21. X. Zheng, B. Chen, C. Wu and S. Priya, *Nano Energy*, 2015, **17**, 269-278.
22. M. Yin, F. Xie, H. Chen, X. Yang, F. Ye, E. Bi, Y. Wu, M. Cai and L. Han, *Journal of Materials Chemistry A*, 2016, **4**, 8548-8553.
23. Y. Zhou, M. Yang, W. Wu, A. L. Vasiliev, K. Zhu and N. P. Padture, *Journal of Materials Chemistry A*, 2015, **3**, 8178-8184.
24. Y. Rong, X. Hou, Y. Hu, A. Mei, L. Liu, P. Wang and H. Han, *Nature Communications*, 2017, **8**.
25. Y. Chen, Y. Zhao and Z. Liang, *Chemistry of Materials*, 2015, **27**, 1448-1451.
26. C. C. Stoumpos, C. D. Malliakas and M. G. Kanatzidis, *Inorganic Chemistry*, 2013, **52**, 9019-9038.
27. T. Baikie, Y. Fang, J. M. Kadro, M. Schreyer, F. Wei, S. G. Mhaisalkar, M. Graetzel and T. J. White, *Journal of Materials Chemistry A*, 2013, **1**, 5628-5641.
28. N. Onoda-Yamamuro, O. Yamamuro, T. Matsuo and H. Suga, *Journal of Physics and Chemistry of Solids*, 1992, **53**, 277-281.
29. P. Whitfield, N. Herron, W. Guise, K. Page, Y. Cheng, I. Milas and M. Crawford, *Scientific reports*, 2016, **6**, 35685.
30. X. Jia, Z. Hu, Y. Zhu, T. Weng, J. Wang, J. Zhang and Y. Zhu, *Journal of Alloys and Compounds*, 2017, **725**, 270-274.
31. J. Borchert, H. Boht, W. Fränzel, R. Csuk, R. Scheer and P. Pistor, *Journal of Materials Chemistry A*, 2015, **3**, 19842-19849.
32. P. Docampo, F. C. Hanusch, N. Giesbrecht, P. Angloher, A. Ivanova and T. Bein, *Apl Materials*, 2014, **2**, 081508.
33. S. Lilliu, T. G. Dane, M. Alsari, J. Griffin, A. T. Barrows, M. S. Dahlem, R. H. Friend, D. G. Lidzey and J. E. Macdonald, *Advanced Functional Materials*, 2016, **26**, 8221-8230.
34. S. Yang, Y. C. Zheng, Y. Hou, X. Chen, Y. Chen, Y. Wang, H. Zhao and H. G. Yang, *Chemistry of Materials*, 2014, **26**, 6705-6710.
35. T. M. Brenner, Y. Rakita, Y. Orr, E. Klein, I. Feldman, M. Elbaum, D. Cahen and G. Hodes, *Chemistry of Materials*, 2016, **28**, 6501-6510.
36. J.-H. Im, I.-H. Jang, N. Pellet, M. Grätzel and N.-G. Park, *Nature Nanotechnology*, 2014, **9**, 927-932.
37. N. Ahn, S. M. Kang, J.-W. Lee, M. Choi and N.-G. Park, *Journal of Materials Chemistry A*, 2015, **3**, 19901-19906.
38. L. Herbet, J. Marquardt, A. Scarpa and J. Blasie, *Biophysical Journal*, 1977, **20**, 245-272.
39. A. Tronin, C.-H. Chen, S. Gupta, D. Worcester, V. Lauter, J. Strzalka, I. Kuzmenko and J. Blasie, *Chemical physics*, 2013, **422**, 283-289.
40. J. Liu, J. Kirchoff, L. Zhou, M. Zhao, M. Grapes, D. Dale, M. Tate, H. Philipp, S. Gruner and T. Weihs, *Journal of synchrotron radiation*, 2017, **24**.
41. H. Joess, J. Brock and A. Woll, *Journal of synchrotron radiation*, 2018, **25**, 706-716.
42. D.-M. Smilgies, *Journal of Applied Crystallography*, 2009, **42**, 1030-1034.
43. N. Cho, F. Li, B. Turedi, L. Sinatra, S. P. Sarmah, M. R. Parida, M. I. Saidaminov, B. Murali, V. M. Burlakov and A. Goriely, *Nature Communications*, 2016, **7**, 13407.

ARTICLE

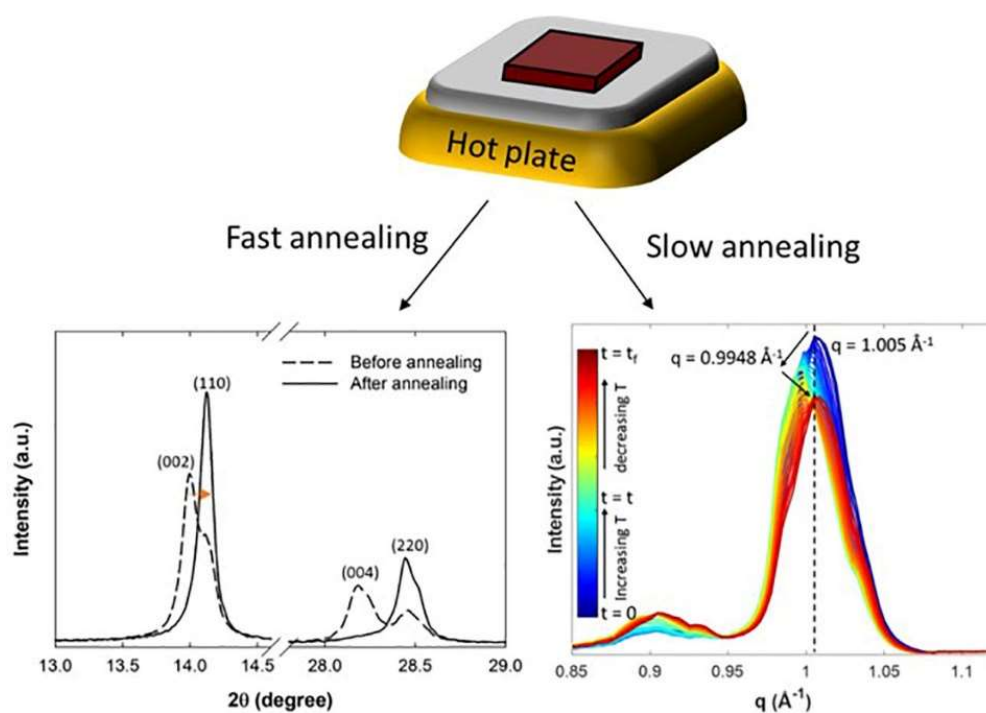
Journal Name

44. J. Feng, *Apl Materials*, 2014, **2**, 081801.
45. H. He, Q. Yu, H. Li, J. Li, J. Si, Y. Jin, N. Wang, J. Wang, J. He and X. Wang, *Nature Communications*, 2016, **7**, 10896.
46. F. Staub, H. Hempel, J.-C. Hebig, J. Mock, U. W. Paetzold, U. Rau, T. Unold and T. Kirchartz, *Physical Review Applied*, 2016, **6**, 044017.
47. A. Sproul, *Journal of Applied Physics*, 1994, **76**, 2851-2854.

Table of Content

Crystal reorientation in methylammonium lead iodide perovskite thin film with thermal annealing

Shalinee Kavadiya^{1,2}, Joseph Strzalka³, Dariusz M. Niedzwiedzki⁴, Pratim Biswas^{1,*}



Two orientations in perovskite ($\text{CH}_3\text{NH}_3\text{PbI}_3$) film, (110) and (002), were resolved and shown to be affected by thermal annealing procedure.